Monthly Notices
of the
ROYAL ASTRONOMICAL SOCIETY

Mon. Not. R. Astron. Soc. **418,** 612–624 (2011) doi:10.1111/j.1365-2966.2011.19510.x

A particle simulation for the global pulsar magnetosphere – II. The case of dipole field

Tomohide Wada[1⋆] and Shinpei Shibata[2⋆]

[1]*National Astronomical Observatory of Japan, Osawa 2-21-1, Mitaka 181-8588, Japan*
[2]*Department of Physics, Yamagata University, Kojirakawa, Yamagata 990-8560, Japan*

Accepted 2011 July 26. Received 2011 July 25; in original form 2010 November 22

ABSTRACT

The main issue regarding the pulsar magnetosphere is how the rotation power is converted into both particle beams which cause pulsed emissions, and a highly relativistic wind of electron–positron plasmas which forms surrounding nebulae shining in X-rays and TeV γ-rays. As a sequel to our previous paper, we carried out a three-dimensional particle simulation for the axisymmetric global magnetosphere. We present the results of additional calculations, which are higher resolution models and higher pair creation rate cases, and a detailed analysis for the solution. We confined our work to demonstrating the cases of low pair creation rates, i.e. where the magnetic field is a fixed dipole. The radiation drag of the plasma was taken to be in a form with the curvature radius along the dipole magnetic field. The electrostatic interactions were calculated using a programmable special-purpose computer, GRAPE-DR. We found that once pair creation begins in the outer gaps, both positively and negatively charged particles begin to drift across the closed magnetic field due to radiation drag, and they create an outflow. Eventually, the steady magnetosphere has outer gaps, both positively and negatively charged outflow of plasma and a region in which the electric field is dominant extending from the equator. In the steady state, the magnetic field generated by the magnetospheric current is comparable to the dipole magnetic field outside several light radii from the star. In a much higher pair creation rate model, the effect of the modification of the magnetic field will bring about modification of the outflow of the plasma, requiring further study with a higher pair creation rate model in a subsequent paper.

Key words: magnetic fields – plasmas – pulsars: general.

1 INTRODUCTION

Rotation-powered pulsars are bright sources in the X-ray sky (e.g. Becker & Trüemper 1997; Possenti et al. 2002; Kargaltsev & Pavlov 2008) and the γ-ray sky (e.g. Nel et al. 1996; de Jager & Djannati-Ataï 2008) as well as in the radio (e.g. Hobbs et al. 2004), and they are identified as magnetized rotating neutron stars. Pulsed emissions originate in the accelerated particles in the magnetosphere. In addition, as a persistent source of high-energy photons, we observe nebulae around young pulsars with synchrotron X-ray radiation (Kargaltsev & Pavlov 2008), inverse Compton TeV radiation (de Jager & Djannati-Ataï 2008) and thermal radiation from the neutron star (Becker & Trüemper 1997). The emission from a nebula is caused by the termination shock of a pulsar wind, which is believed to be the relativistic outflow of magnetized pair plasmas transporting out most of the rotation power (Rees & Gunn 1974; Kennel & Coroniti 1984a,b). However, the nature of the pulsar wind and that of the radiation beam from the pulsar magnetosphere have long remained unexplained. As a primitive model, Goldreich & Julian (1969, hereafter GJ) suggested an axisymmetric steady model of the pulsar magnetosphere in which the neutron star is assumed to be a perfect conductor surrounded everywhere by charge-separated force-free plasmas. The model assumes that the plasma corotates with the star in the light cylinder, although this corotational magnetosphere can be violated beyond the light cylinder. Then the GJ model assumes that the plasma is replaced by acceleration along the opened magnetic field line beyond the light cylinder. On the basis of the copious plasma in the magnetosphere, global relativistic magnetodynamics models are applied to help us explain the acceleration of the pulsar wind (Bucciantini et al. 2006; Komissarov 2006; McKinney 2006a,b) and possible dissipation such as in magnetic neutral sheets may contribute to high-energy pulsed radiation (Kirk, Skjæraasen & Gallant 2002). In comparison with these studies, several other studies have shown that an aligned

⋆E-mail: tomohide.wada@nao.ac.jp (TW); shibata@sci.kj.yamagata-u.ac.jp (SS)

rotating neutron star should consist of electrostatically charged clouds surrounded by vacuum gaps without pulsar wind, and therefore the steady solutions with outflow of plasma are not self-consistent (see Michel & Smith 2001). Concerning the electrostatic solution, Krause-Polstorff & Michel (1985a,b, hereafter KMab) performed a particle simulation for the axisymmetric model and showed formation of gaps around the null surface with a rotating equatorial disc and polar domes. This model suggests a quiet electrosphere when the plasma is extracted only from the stellar surface, but the vacuum gap in the middle latitudes looked to be unstable against the pair-creation cascade. Subsequently Smith, Michel & Thacker (2001) reconstructed the same result with a higher accuracy, and even if the pair plasma was generated in the gaps at the middle latitudes, the quiet solution without pulsar wind was identified. In their models, the quiet solution is obtained when the particles are located at equilibrium positions along the dipole magnetic field line, and this picture is valid if the plasma is placed fully inside the light cylinder and the magnetic field is larger than the electric field. In other words, the effects of the inertia of the corotational plasma around the light cylinder are not considered. The same result was obtained by Pétri, Heyvaerts & Bonazzola (2002a) who concluded that a given total charge of the system determined by the net outgoing charged flux and the potential configuration is unfavourable for the particles to escape to infinity such as in the active solution obtained by a magnetohydrodynamics (MHD) approximation. However, the quiet solution should be modified to consider the leakage of plasma when the electrostatic plasma is in the vicinity of the light cylinder. Investigating the possibility of a radial outflow from the equatorial disc on the equator, Spitkovsky (2004) discovered the leaking mechanism of the equatorial disc caused by the diocotron instability with numerical simulation, which was also pointed out by Pétri, Heyvaerts & Bonazzola (2002b) with linear theory. The leakage of the disc should be significant so as to create the current in the vacuum region outside the quiet electrosphere. But the time-scale of diffusion of the plasma in the vicinity of the light cylinder is much larger than the rotation period, and therefore further study is needed to follow the global current structure over a much longer time-scale, such as a global numerical simulation with much more computational time and relativistic kinematics.

Contrary to the previously reported quiet solutions, we reported in our previous paper an active solution (Wada & Shibata 2007, hereafter, WS) with coexisting pulsar wind and outer gaps in which the effects of the inertia and radiation drag for the plasma are included by three-dimensional particle simulation in a special relativistic regime, and the simulation starts from the quiet solution of KMab. Once pair plasmas are generated in the vacuum gaps around the quiet electrosphere, a positively charged outflow forms near the equator and a negatively charged outflow forms in the polar region of the star. The outflow of plasma serves to maintain the charge deficiency in the outer gaps. To balance the loss and maintain the supply of particles from the outer gaps, the magnetosphere eventually settles into a steady state with pulsar wind. But there remain some problems to be solved. At first, although our simulation showed that the wind coexists with the pair-creating regions in the pulsar outer magnetosphere, the solution is only obtained by the lowest pair creation rate, where we carried out a simulation in which the current density around the star is less than that of the GJ model, and therefore the magnetic field from the magnetospheric current is negligibly small in the light cylinder. If the pair creation rate is assumed to gradually become large in our simulation, the gaps tend to reduce and decrease the generation rate of the plasma, and therefore the active structure might disappear. Although the drift motion of plasma caused by the radiation drag force works as a leaking mechanism in a closed magnetic field and is favourable to maintain the outer gaps, a recalculation would be needed to find out whether our active solution is maintained in higher pair creation rate models. Secondly, the obtained structure of the outer gaps contains some artefacts due to the accuracy. The detailed flow pattern of the plasma such as the poloidal current loop inside the light cylinder was not clear because of the low resolution of our previous work. We will simulate the lowest pair creation rate model again with a higher resolution in which the unit charge of a particle is taken to be 1/10. Finally, our particle simulation has a numerical error, which is defined as the resolution of the charge of simulation particles and the injection of the plasma from the inner boundary. In our previous work (WS), the polar potential drop is maintained at a factor of 3 times larger than the artefact level; however, the present higher resolution model will decrease the error and confirm the existence of the polar potential drop. However, the particles that we consider have a large inertia length which is about 3 per cent of the stellar radius, and therefore we infer that our simulation could not resolve the size of the polar cap accelerator.

Meanwhile, to investigate the development of a global magnetosphere, some phenomenological models that concern the local structure of magnetospheric activity have been developed: the polar cap models (Ruderman & Sutherland 1975; Arons & Scharlemann 1979; Zhang & Harding 2000; Harding & Muslimov 2002), the outer gap models (Holloway 1973; Cheng, Ho & Ruderman 1986a,b; Romani 1996; Zhang & Cheng 1997; Hirotani & Shibata 1999; Takata et al. 2006) and the slot gap model (Muslimov & Harding 2003, 2004). These models have been developed to explain the observed pulsed light curve and spectrum. The critical point with these models is how the electric field along the magnetic field, $E_{\parallel}$, is maintained locally although the existence of the gap is implicit in these models. Although the adequacy of these gap models is achieved statistically by many further observations, these models usually contain many degrees of freedom, for example, which are the surface magnetic field intensity of the pulsar, the inclination angle between the magnetic axis and rotational axis, the viewing angle from the gaps and so on. Recently, radiation from the pulsar magnetosphere with high-energy γ-ray bands has been observed by the *Fermi* γ-ray telescope, and 38 γ-ray pulsars have been discovered (Abdo et al. 2009a,b, 2010) of which 21 are radio-loud and 17 are radio-quiet. These observations could discriminate between emission models located in the polar region or in the outer region, i.e. polar cap, slot gap and outer gap. The *Fermi* telescope has also measured the spectral properties above 10 GeV with a better sensitivity than EGRET. It was found that the spectral shape of γ-ray emissions from the Vela pulsar is well fitted with a power law (photon index $\Gamma \sim 1.5$) plus exponential cut-off ($E_{\rm cut} \sim 3$ GeV) model. The discovered exponential cut-off feature predicts that emissions from the outer magnetosphere (Abdo et al. 2009c) are more favoured than from the polar cap region (Daugherty & Harding 1996), which predicts a superexponential cut-off with magnetic pair creation. Furthermore, using the MAGIC (Major Atmospheric Gamma Imaging Cherenkov) telescope, the detection of the radiation above the 25 GeV bands associated with the Crab pulsar has also predicted a high-energy emission in the outer magnetosphere (Aliu et al. 2008).

In this paper, we develop our global model of linking the outer gap with the pulsar wind. In order to obtain a solution, we utilize a particle simulation in which particle motion and electric field are alternately solved in the same way as the particle-in-cell (PIC) methods, but using the magnetic field with dipole in our present

model. We simulate the generation of the plasma by pair creation in the gap and then obtain a steady state of the axisymmetric magnetosphere by solving the equation of motion including drag force due to curvature radiation and the electromagnetic fields. Since the motion of the individual particles is tracked, we can simulate any kind of drift motions for plasma, arising from the radiation drag force, the centrifugal force and the gradient of the magnetic field: $\boldsymbol{f}_{\rm ext} \times \boldsymbol{B}$ drift, $\boldsymbol{E} \times \boldsymbol{B}$ drift and magnetic gradient drift. Here, we provide results of additional calculations and a detailed analysis for our steady solutions. We will show that the trans-field drift by radiation drag plays an important role, and eventually the electric field dominant region expanding to both sides of the equatorial plane makes a global poloidal current loop. But this paper considers cases with a low rate of pair creation, and therefore here we will avoid a modification of the original dipole field as we also did in our previous work. First, the previous result (WS) of our steady solution was reconstructed with 10 times the number of particles, and models with several pair creation rates were run. Our methods of calculation for the particle simulation are given in Section 2, the results are presented in Section 3 and a discussion is presented in Section 4.

2 NUMERICAL METHOD

2.1 Outline

We solve the motion of the particles and the electromagnetic field alternately so as to obtain a self-consistent steady structure of the electromagnetic field and particle distribution. This method is similar to the well-established PIC method. However, to obtain a steady solution, we use static solutions of the Maxwell equations, i.e. we omit the effects of time variation of the field ($\partial \boldsymbol{E}/\partial t = \partial \boldsymbol{B}/\partial t = 0$). This enables us to use the programmable special-purpose computer for astronomical N-body problems, GRAPE-DR (Makino, Hiraki & Inaba 2007), which calculates Coulomb interaction very fast with a high degree of precision at the position of the plasma.

In our simulation, the generation of the particle is considered, which is not common in PIC methods. There are two cases: (1) electrons or protons on the stellar surface pop into the magnetosphere due to the unipolar induced electric field of the star; (2) electron–positron pairs are created due to photon–photon collision or magnetic pair creation in the magnetosphere. For simplicity, the masses of both the positively and negatively charged simulation particles are assumed to have the same value, that is, the proton and positron are not distinguished, and the type of pair creation is not distinguished, that is, the detailed process of pair creation is not considered. We assume the pulsar to be a rotating spherical conductor in which the magnetic field is uniform with the magnetized axis being parallel to the rotation axis. In this paper, because we consider the case of a low rate of pair creation, which has much less current density than the GJ model inside the light cylinder, the modification of the dipole magnetic field near the star by the magnetospheric current would be trivial. For this reason, the magnetic field outside the star is assumed to be a dipole, i.e.

$$\boldsymbol{B} = \frac{\mu}{r^3}(2\cos\theta \boldsymbol{e}_r + \sin\theta \boldsymbol{e}_\theta), \tag{1}$$

where θ is the colatitude, r is the distance from the centre of the star, $\mu = B_0 R^3/2$ is the dipole magnetic moment, B_0 is the magnetic field intensity at the poles, R is the stellar radius, and $\boldsymbol{e}_r$ and $\boldsymbol{e}_\theta$ are the unit vectors along the r and θ directions, respectively. These assumptions give the electric potential on the stellar surface:

$$\phi(\boldsymbol{R}) = \frac{\Omega\mu \sin^2\theta}{cR} + \text{constant}, \tag{2}$$

where Ω is the angular velocity of the star. This provides the inner boundary condition for the Poisson equation for the electric potential.

If the outside of the star is a vacuum, the electrostatic potential given by the solution of the Laplace equation $\nabla^2\phi = 0$ is

$$\phi_{\rm v} = \phi_1 + \phi_4, \tag{3}$$

where

$$\phi_1 = \frac{Q_{\rm sys}}{r}, \tag{4}$$

$$\phi_4 = -\frac{\mu\Omega R^2}{3cr^3}(3\cos^2\theta - 1), \tag{5}$$

and $Q_{\rm sys} = \alpha 2\mu\Omega/(3c)$, where α is the non-dimensional net charge of the system. If we follow Jackson's Gedanken experiment (Jackson 1976), we choose $\alpha = 1$ as an initial condition, which corresponds to the +10 model for KMab. Consequently, the vacuum electric field becomes

$$\boldsymbol{E}_{\rm v}(\boldsymbol{r}) = -\nabla\phi_{\rm v} = \boldsymbol{E}_4(\boldsymbol{r}) + \boldsymbol{E}_1(\boldsymbol{r}), \tag{6}$$

where

$$\boldsymbol{E}_4(\boldsymbol{r}) = -\frac{\mu\Omega R^2}{cr^4}(3\cos^2\theta - 1)\boldsymbol{e}_r - \frac{\mu\Omega R^2 \sin 2\theta}{cr^4}\boldsymbol{e}_\theta, \tag{7}$$

$$\boldsymbol{E}_1(\boldsymbol{r}) = \frac{Q_{\rm sys}}{r^2}\boldsymbol{e}_r. \tag{8}$$

This vacuum solution has the surface charge density where

$$\sigma_{\rm v} = \frac{\mu\Omega}{4\pi cR^2}(3 - 5\cos^2\theta) + \frac{Q_{\rm sys}}{4\pi R^2}. \tag{9}$$

Given B_0, R and the light speed c, all quantities in our simulation are normalized. In the following, barred quantities indicate normalized values. For example, electric charge is measured in the unit of B_0R^2, and $\bar{Q}_{\rm sys} = Q_{\rm sys}/B_0R^2$. In the following subsections, we describe the detailed method of our simulation.

2.2 Method of solution for the electric field

The space charge density in the magnetosphere is represented by a limited number of simulation particles, i.e.

$$\rho_{\rm m}(\boldsymbol{r}) = \sum_{i=1}^{n} q_i \delta(\boldsymbol{r} - \boldsymbol{r}_i). \tag{10}$$

In the simulation, we are concerned with superparticles which have the same mass and opposite sign of charge with the same absolute value of the charge, and therefore the difference in the mass of the ion and that of the positron is not considered. As we introduce later, the normalized values of the mass and charge for the superparticle are represented by $\bar{m}$ and $\bar{q}$, respectively. The electric potential in the magnetosphere is determined by Poisson's equation, i.e. the solution for the electric potential is given by the superposition of the vacuum component (3) and the space charge component, which is calculated by $-\nabla^2\phi_{\rm m} = \rho_{\rm m}$, with the boundary condition $\phi_{\rm m}(\boldsymbol{R}) = 0$, and we have

$$\phi_{\rm m}(\boldsymbol{r}) = \sum_{i=1}^{n} q_i \left[\frac{1}{|\boldsymbol{r} - \boldsymbol{r}_i|} - \frac{R/r_i}{|\boldsymbol{r} - (R/r_i)^2\boldsymbol{r}_i|} - \left(1 - \frac{R}{r_i}\right)\frac{1}{r}\right] \tag{11}$$

for the electric potential,

$$\boldsymbol{E}_{\rm m}(\boldsymbol{r}) = \sum_{i=1}^{n} q_i \left[\frac{\boldsymbol{r}-\boldsymbol{r}_i}{|\boldsymbol{r}-\boldsymbol{r}_i|^3} - \frac{R}{r_i}\frac{\boldsymbol{r}-(R/r_i)^2\boldsymbol{r}_i}{|\boldsymbol{r}-(R/r_i)^2\boldsymbol{r}_i|^3} - \left(1-\frac{R}{r_i}\right)\frac{\boldsymbol{r}}{r^3}\right] \tag{12}$$

for the electric field, and

$$\sigma_{\rm m} = \sum_{i=1}^{n} q_i \left[\frac{1}{4\pi R}\frac{R^2-r_i^2}{|\boldsymbol{R}-\boldsymbol{r}_i|^3} - \frac{1}{4\pi R^2}\left(1-\frac{R}{r_i}\right)\right] \tag{13}$$

for the surface charge density. Thus, the solution of the electric field with the boundary condition (2) is given in the following forms:

$$\phi = \phi_{\rm m} + \phi_{\rm v}, \tag{14}$$

$$\boldsymbol{E} = \boldsymbol{E}_{\rm m} + \boldsymbol{E}_{\rm v}, \tag{15}$$

$$\sigma = \sigma_{\rm m} + \sigma_{\rm v}. \tag{16}$$

2.3 Popping of particles from the stellar surface

GJ pointed out that the rotation-induced electric field pulls charged particles from the stellar surface against the gravitational force. In the following, we describe how this process is realized in our simulation.

In vacuum conditions, the scalar product of the electric field and the magnetic field on the stellar surface is given by

$$\boldsymbol{E}\cdot\boldsymbol{B} = \frac{\Omega R B_0^2}{c}\cos\theta\left(\frac{\alpha}{3}-\cos^2\theta\right). \tag{17}$$

The sign of the electric field along the magnetic field ($E_\parallel$) changes on the surfaces $\cos\theta = \pm\sqrt{\alpha/3}$, i.e. the negatively charged particles pop out from the polar region and the positively charged particles pop out from the equatorial region. Once the charge is emitted from the stellar surface, they experience $E_\parallel$ which changes the sign of $r = R + \sqrt{3/\alpha}\cos\theta$ for the electron or of $\theta = \pi/2$ for the positron and ion (see Jackson 1976). The electrons that are emitted from the lower colatitude region are accelerated outwards along the magnetic field line at first. For the electrons, after passing over the surface at which the minimum of the potential energy is given, the field-aligned electric field decelerates the particles and they are reflected towards the stellar surface again. Then they accumulate near the surface and make a polar dome of electrons because of the radiation drag force exerted by the curvature radiation for the particle. At the same time, positrons or protons are emitted from the higher colatitudes accumulating on the latter surface, i.e. the equatorial plane, and making an equatorial positively charged torus. Thus, the vacuum electric field tends to be screened out by the particles in the magnetosphere.

If the surface electric field along the magnetic field is shielded, the surface charge density becomes

$$\sigma_{\rm GJ} = \frac{3}{8\pi}\frac{B_0\Omega R}{c}\sin^2\theta. \tag{18}$$

This surface charge density results in a kink of the magnetic field from the uniform one inside to the dipole one outside under the ideal MHD condition. Although the surface charge density appearing on the stellar surface is σ, only the excess charge $\sigma - \sigma_{\rm GJ}$ is emitted from the stellar surface and therefore we expect that the surface charge density becomes $\sigma_{\rm GJ}$ in the steady condition. Thus, we replace $\sigma - \sigma_{\rm GJ}$ by the movable simulation particle. For simplicity, the work function of the particles on the stellar surface is not considered, that is the free emission of particles is assumed.

2.4 Parameter setting

In our simulation, we use a superparticle with artificially enlarged mass and charge of $\bar{q} = 10^{-5}$, $\bar{m} = 10^{-10}$ or $\bar{q} = 10^{-6}$, $\bar{m} = 10^{-11}$. The number of particles representing the charge $\rho_{\rm GJ,pole}R^3$ is about 10^4 particles for the $\bar{q} = 10^{-5}$ model, which is the same as that used in WS, and 10^5 particles for the $\bar{q} = 10^{-6}$ model, respectively. The actual number of particles increases because of pair creation, the total number of particles in the simulation domain jumps 10-fold for them and therefore it needs an extensive calculation related to the square of the number of particles for the Coulomb interaction in one step. Thus, we gain the privilege of using GRAPE-DR, which is a programmable special-purpose computer for astronomical N-body problems, to calculate the interaction between the particles.

In a realistic pulsar magnetosphere, the minimum scale of the motion of the plasma is the gyroradius, which is $r_{\rm g} = 1.7 \times 10^{-2} r_3 \gamma_7$ cm for an electron or a positron, where γ is the Lorentz factor of the particle, $r_3 = (r/R)^3$, and $\gamma_7 = \gamma/10^7$. We use superparticles with a larger mass–charge ratio than the real one. We take $\bar{\Omega} = 0.2$ and $\bar{m}/\bar{q} = 10^{-5}$. For the definition of the numerical parameters, a typical gyroradius of a simulation particle on the pole is set to be 10^{-5} stellar radii, and therefore the corresponding time-step is set at $\mathrm{d}\bar{t} = 10^{-5}$. Since the valid time-step of the particle for the gyromotion increases proportionately to the distance cubed from the star $\sim \bar{r}^3$, we use the individual time-step for each simulation particle adapted to the position to reduce the total step number of the integration for the trajectory of the particle. As we introduce the size of the numerical domain later, we have to follow these particles over several dynamical time-lengths of the simulation domain until a steady condition is achieved. It takes about six rotation periods of the star, i.e. $\bar{t}_{\rm sim} \sim 200$.

For the unipolar induced electric potential by the rotational magnetized conductor, the available maximum energy of the particle is estimated by the open field line voltage

$$\phi_{\rm eff} = \frac{\mu\Omega^2}{c^2} = 1.6\times10^{14}\left(\frac{P}{0.2\,\mathrm{s}}\right)^{-2}\ \mathrm{V}, \tag{19}$$

which gives the maximum Lorentz factor of

$$\gamma_{\rm max} = \frac{q\mu\Omega^2}{mc^4} = 3.2\times10^{8}\left(\frac{P}{0.2\,\mathrm{s}}\right)^{-2} \tag{20}$$

for electrons and positrons. Note that if the Lorentz factor of a particle becomes $\gamma_{\rm max}$, the gyroradius in the vicinity of the light cylinder becomes the same order of the light radius. In other words, as expected, the localized acceleration region has a much smaller potential drop than $\phi_{\rm eff}$, the gyroradius of the particles is much smaller than the light radius. In our simulation, the gyroradius $\bar{r}_{\rm g}$ of all accelerated superparticles is guaranteed to be smaller than the size of the light radius; typically $\bar{r}_{\rm g} = 10^{-2}\bar{R}_{\rm l}$ for an accelerated particle corresponds to the Lorentz factor $0.1\gamma_{\rm max}$ at the light radius.

2.5 Inner and outer boundaries

For the injection of the particles from the stellar surface, the surface charge $(\sigma - \sigma_{\rm GJ})\Delta S$ is replaced by the simulation particles, where ΔS is the surface element of the stellar surface. If the particles are set on the stellar surface, they are pulled back by the mirror charge, i.e. the second term of (12). If this attractive field is larger than the induced electric field, it prevents extraction of particles from the stellar surface as an artificial work function. Then the assumption of free emission of the particle from the stellar surface is not proved. We put the particles above the altitude of $\bar{h}_{\rm c}$ from the stellar surface

to avoid this artificial attractive force. We chose $\bar{h}_c = 0.04$ for the $\bar{q} = 10^{-5}$ model and $\bar{h}_c = 0.013$ for the $\bar{q} = 10^{-6}$ model. If the particles go back into the sphere with radius $r = R + \bar{h}_c$, the particles are deleted in the numerical region. It is notable that a numerically thin vacuum layer does not change the result at all.

To conserve the total number of simulation particles, we remove the particles beyond a sphere with radius R_{OB} and the removed charge is reduced from Q_{sys}. The size of the outer boundary is taken to be larger than that of the accelerating region ($\sim R_l$), that is, we chose $R_{OB} = 10R_l$. In our simulation, the removed particles beyond the outer boundary have positive total energy (kinetic plus potential), and we reckon they would outflow. To examine the effect of the size of the outer boundary, larger outer boundary models, which are $R_{OB} = 20R_l, 30R_l$, were investigated, from which we confirmed that the structure of the magnetosphere inside the sphere with radius $8R_l$ is not affected by the sizes of the outer boundaries. Thus, we use $R_{OB} = 10R_l$ as our standard model.

2.6 Particle motion

The equation of motion of the particles is given by

$$m_i c \frac{\mathrm{d}\gamma_i \boldsymbol{\beta}_i}{\mathrm{d}t} = q_i \left[\boldsymbol{E}(\boldsymbol{r}_i) + \boldsymbol{\beta}_i \times \boldsymbol{B}(\boldsymbol{r}_i) \right] + \boldsymbol{f}_{\mathrm{rad},i}, \tag{21}$$

where m_i, q_i, $\boldsymbol{r}_i$ and $\boldsymbol{\beta}_i$ are the mass, the charge, the position and the velocity of the ith particle, and $\boldsymbol{f}_{\mathrm{rad},i}$ represents the drag force due to the curvature radiation of the accelerated particles. In this paper, the magnetic field is not deformed by the magnetospheric current. The radiation drag force of the particles is given by

$$\boldsymbol{f}_{\mathrm{rad},i} = -\frac{2}{3}\frac{q_i^2}{R_c^2}\gamma_i^4 \frac{\boldsymbol{p}_i}{|\boldsymbol{p}_i|}, \tag{22}$$

where R_c is the curvature radius along a dipole magnetic field line at the position of the particle. Substituting $\varpi^2/r^3 = 1/r_{eq} = \text{constant}$, the curvature radius is given by

$$R_c = f\frac{r}{3\sin\theta} \quad \text{with} \quad f = \frac{(4 - 3r/r_{eq})^{3/2}}{2 - r/r_{eq}}, \tag{23}$$

where r_{eq} is the axial distance of the point at the intersection of the dipole magnetic field line and the equatorial plane. Because $1 < f < 4$ with $0 < r/r_{eq} < 1$, we take $R_c = 4r/(3\sin\theta)$ approximately.

If the Lorentz factor of the particle increases, (22) becomes comparable to the Lorentz force, and such a particle has $\boldsymbol{f}_{\mathrm{rad}} \times \boldsymbol{B}$ drift motion crossing the dipole magnetic surface. The critical Lorentz factor for this effect is given by

$$\gamma_d = \left(\frac{3\pi\mu}{qcP}\right)^{1/4}. \tag{24}$$

For a realistic pulsar magnetosphere, it corresponds to $\gamma_d = 3.6 \times 10^7 P_{0.2}^{-1/4}(R_c/R_l)^{1/2}$. Considering the dependence of the distance for R_c, $R_c \sim R_l$ in the vicinity of the light cylinder. For electrons, $\gamma_d/\gamma_{max} = 0.11$ with $P = 0.2\,\mathrm{s}$ and $\mu = 10^{30}\,\mathrm{G\,cm^3}$, and thus the particles accelerated with 11 per cent of the open field line voltage suffer from such a drift motion. On the other hand, for our simulation particles, $\gamma_{d,sim}/\gamma_{max,sim} = 0.0055$ for the $\bar{q} = 10^{-5}$ model and $\gamma_{d,sim}/\gamma_{max,sim} = 0.0098$ for the $\bar{q} = 10^{-6}$ model, i.e. once the kinetic energy of particles become 1 per cent of $q\phi_{max}$, the radiation drag force becomes comparable to the Lorentz force. As a result, the radiation drag force for the superparticle would be exaggerated. To perform the radiation drag force properly, we introduce the reduction factor η, namely γ_i in (22) is replaced by $\eta\gamma_i$ and we take $\eta = 0.05$ for the $\bar{q} = 10^{-5}$ model and $\eta = 0.089$ for the $\bar{q} = 10^{-6}$ model although we simulated with $\eta = 1$ in our previous work.

2.7 A test run: reproduction of a quiet solution

The pair creation in the gap has a significant role in the structure of the magnetosphere. If pair creation is suppressed, the static magnetosphere by KMab is reproduced. Following Jackson's Gedanken experiment (Jackson 1976), our simulation starts with the condition that the positively charged magnetized rotating conductive sphere is initially put at the origin in a vacuum. Charge-separated particles are emitted from the stellar surface and are accelerated by the induced electric field along the magnetic field lines. But the energy of the particles is lost due to the radiation drag force with time. The particles are located at the bottom of the potential along the magnetic field line, i.e. the force-free surfaces where the magnetic field aligned electric field vanishes. In a vacuum, the force-free surfaces are polar domes and the equatorial plane. The insides of the polar force-free surfaces are filled with the negative charges emitted from the polar caps of the stellar surface, and they extend upwards and form north and south force-free domes. Similarly, the positive particles accumulate above and below the equatorial plane and form a force-free torus. Eventually the field-aligned electric field on the stellar surface is shielded, and the static negatively charged domes above the poles and the static equatorial positively charged disc are formed. Fig. 1 shows the static particle distribution with the equipotentials ϕ. For comparison, they are superposed on the corotational equipotentials which are given by $\phi_{co} = \Omega\psi/c$, where $\psi = \mu\sin^2\theta/r$ is the dipole magnetic flux function. The equipotentials follow the corotational equipotentials in the negatively charged clouds and the inner part of the positively charged torus close to the stellar surface. In the cusp of the torus, the two kinds of equipotentials deviate but they are parallel. Roughly, positively and negatively $E_\parallel$ is screened

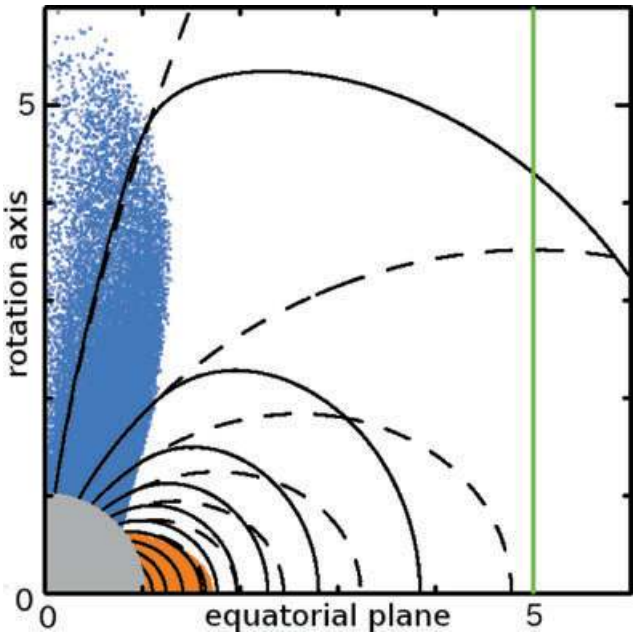

Figure 1. The particle distribution and the equipotentials for the $\alpha = 1$ and $q_{unit} = 10^{-6}$ model. The orange and cyan points are positive and negative particles on the meridional plane (ϖ, z), respectively. The light cylinder is located at $\varpi = 5$ as shown by the green line. The broken lines are the corotational equipotentials. The solid lines are the equipotentials. The contour level is considered to have an equal interval at $0.5\phi_{eff}$.

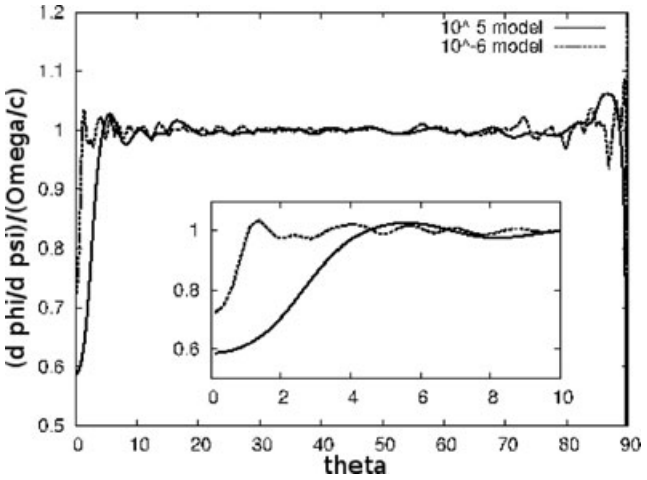

Figure 2. $\mathrm{d}\phi/\mathrm{d}\psi$ normalized by Ω/c versus the colatitude on the inner boundary. The small panel is a close up near the polar region from 0° to 10°.

out in both the charged clouds. Meanwhile, the electric field in the vacuum region faces a direction such that particles are drawn back to the cloud with the same sign of charge, and therefore the cloud–vacuum boundaries remain stable.

The force-free plasma in the cloud has a toroidal velocity by $\boldsymbol{E} \times \boldsymbol{B}$ drift, which is given by

$$v_{\mathrm{t}} = \varpi\Omega + c\varpi\frac{\mathrm{d}\phi_{\mathrm{nco}}}{\mathrm{d}\psi}, \tag{25}$$

where ϖ is the radius in the cylindrical coordinates and $\phi_{\mathrm{nco}} \equiv \phi - \phi_{\mathrm{co}}$. The coincidence of ϕ and ϕ_{co} in the cloud means $\mathrm{d}\phi_{\mathrm{nco}}/\mathrm{d}\psi = 0$, i.e. corotational motion of the plasma. The values of the potentials fall off faster than the corotational one in the outer part of the disc, and therefore the term $c\varpi\,\mathrm{d}\phi_{\mathrm{nco}}/\mathrm{d}\psi$ gives super-rotation in (25). In this structure, the toroidal velocity of the plasma in the outer part of the disc was less than the light speed because the size of the disc is much less than that of the light cylinder.

As mentioned in Section 2.5, note that our simulation has an artificial thin vacuum layer between the inner boundary and the stellar surface. The region causes deviation of the toroidal velocity from corotation in the polar dome. Fig. 2 shows $\mathrm{d}\phi/\mathrm{d}\psi$ for the 10^{-5} model and the 10^{-6} model in units of Ω/c on the inner boundary. This curve has a symmetry on both sides of the equator. Most of the cloud corotates except for near the poles and the equator. The maximum deviation from the corotational velocity is 40 per cent for the 10^{-5} model and 30 per cent for the 10^{-6} model, respectively. Although the error is large on the equatorial plane, the effect near the equator is trivial because the corotational velocity is originally small at this location. But the deviation by the numerical error near the pole is significant if polar electric domes expand in the vicinity of the light cylinder. In our simulation, the polar force-free electric dome, which connects to the stellar surface along the magnetic field anchored at 3° for the 10^{-5} model and 1° for the 10^{-6} model, has a subrotational velocity that is 90 per cent of the light speed at the distance of the light radius from the star.

2.8 The treatment of pair creation and initial conditions

Fig. 3 shows the distribution of the strength of the electric field along the magnetic field line ($E_\parallel$) on the meridional plane for the static solution. A strong intensity region appears in the middle latitudes, while a weaker intensity appears in the charged clouds.

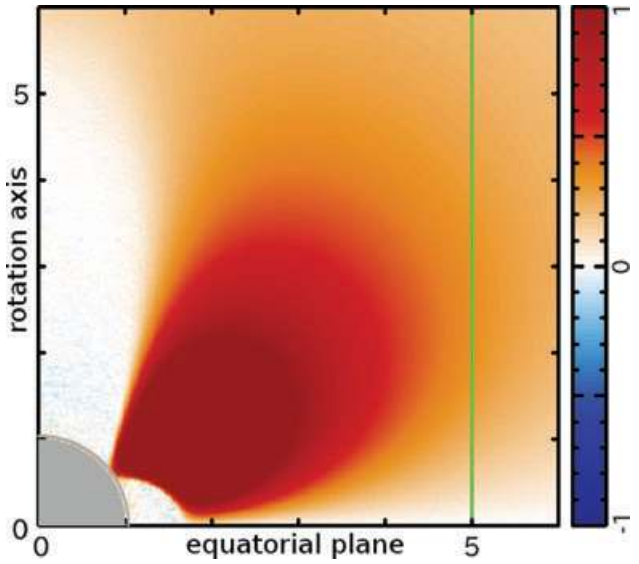

Figure 3. The $E_\parallel$ intensity map for the pair-starved static structure with the $\bar{q} = 10^{-6}$ model on the meridional plane, where the colour intensity is normalized by B_{l}. The light cylinder is located at $\varpi = 5$ as shown by the green line.

For the static solution, there is a vacuum gap in the middle latitudes with a potential drop of $\sim 2\phi_{\mathrm{eff}}$. In the vacuum gap, the maximum intensity of $E_\parallel$ is typically $E_{\parallel,\max} \sim 3B_{\mathrm{l}}$ at $(\varpi, z) = (1.8R, 1.4R)$ on the meridional plane, where $B_{\mathrm{l}} \equiv \mu/R_{\mathrm{l}}^3$ is the dipole magnetic field intensity at the light radius on the equator. If the charged particles are injected into the gap, they will be immediately accelerated to the ultrarelativistic regime by $E_\parallel$, and radiate γ-rays by the curvature radiation process, whose power is given by

$$\dot{\epsilon}_{\mathrm{c}} = \frac{2q^2\gamma}{3R_{\mathrm{c}}^2}. \tag{26}$$

The typical Lorentz factor of the accelerated particles is estimated by the force balance between the radiation drag force and the electric force, i.e. $qE_\parallel = \dot{\epsilon}_{\mathrm{c}}/c$, which gives

$$\gamma_{\mathrm{sat}} = \left(\frac{3\mu R_{\mathrm{c}}^2}{2qR_{\mathrm{l}}^3}\right)^{1/4}. \tag{27}$$

Then, the typical energy of the emitted γ-rays is given by

$$\epsilon_\gamma = \frac{3hc\gamma_{\mathrm{sat}}^3}{4\pi R_{\mathrm{c}}}. \tag{28}$$

With typical parameters of the pulsars, we obtain a Lorentz factor of $\gamma_{\mathrm{sat}} = 1.1 \times 10^6 P_{0.2}^{1/2}(R_{\mathrm{c}}/R_{\mathrm{l}})^{1/2}(E_\parallel/B_{\mathrm{l}})^{1/4}$ and a photon energy of $\epsilon_\gamma = 1.4 \times P_{0.2}^{3/2}(R_{\mathrm{c}}/R_{\mathrm{l}})^{1/2}(E_\parallel/B_{\mathrm{l}})^{3/4}$ GeV. In the present work, we simplify the pair-creation process, that is, (1) we do not distinguish between the photon–photon pair-creation process and the magnetic pair-creation process, and (2) we ignore the effects of the collision angle between the γ-rays and soft-photons (or the magnetic field). In our simulation, we determine the pair-creation position using the condition that $\epsilon_\gamma > 2mc^2$, implying that the pair creation occurs at the position where the electric field is stronger than $E_{\mathrm{cr}} = 6.6 \times 10^{-5} P_{0.2}^2 (R_{\mathrm{c}}/R_{\mathrm{l}})^{2/3} B_{\mathrm{l}}$. $\epsilon_\gamma > 2mc^2$ is not applicable in reality because of the effect of collision angle of the two photons. On the other hand, we will see below that the actual setting of the value of E_{cr} is much larger than this value in the numerical simulation since the accuracy of the electric field is much greater than E_{cr}.

For our simulation, the pair creation is performed in the following way. We introduce the critical electric field intensity to

Table 1. The numerical parameters of the simulations.

Name	$\bar{q}$	$\bar{E}_{\rm cr}$	$\tau_{\rm pr}$	Δr	$\Delta\theta$
A_0	10^{-5}	10^{-3}	2.0	0.1	2°
A_1	10^{-5}	10^{-3}	1.0	0.1	2°
A_2	10^{-5}	10^{-3}	0.2	0.1	2°
A_3	10^{-5}	10^{-3}	0.1	0.1	2°
A_4	10^{-5}	5×10^{-4}	2.0	0.1	2°
A_5	10^{-5}	2.5×10^{-4}	2.0	0.1	2°
B_0	10^{-6}	10^{-3}	0.2	0.1	1°

generate pairs in the simulation as parameters, that is $\bar{E}_{\rm cr}/\bar{B}_{\rm l} = 0.25,\ 0.125,\ 0.0625$ although they are larger than the realistic value. At first, the equally spaced grid points $(\bar{r}_i, \theta_j)$ are prepared with spherical coordinates in the meridional plane, where $\Delta\bar{r} = 0.1$, $\Delta\theta = 2^\circ$ for the $\bar{q} = 10^{-5}$ model and $\Delta\bar{r} = 0.1$, $\Delta\theta = 1^\circ$ for the $\bar{q} = 10^{-6}$ model. If the field-aligned electric field at a grid point $\bar{E}_\parallel(i, j)$ is larger than $\bar{E}_{\rm cr}$, then we place $n_\pm = n_{\rm M}$ pairs around the grid, where $n_{\rm M}$ is the multiplicity of pair creation. The generation of pairs is repeated in every $\bar{\tau}_{\rm pr}$, where we take $\bar{\tau}_{\rm pr} = 2.0, 1.0, 0.2$, which are less than the light-crossing time of the light radius. We consider $n_{\rm M}$ as a constant parameter and the lowest cases $n_{\rm M} = 1$ are carried out to guarantee the pure dipole magnetic field assumption. We set up the static solution as an initial condition of the simulation with the pair-creation effect, e.g. 3000 pairs are generated in the gaps with the $\bar{q} = 10^{-5}$ model, beginning with $n_{\rm M} = 1$. Table 1 provides the numerical set of parameters of the simulation.

Note that the perturbation of a simulation particle gives rise to errors of the electric field. The maximum error of the electric field caused by a simulation particle is roughly given by $E_{\rm err} = \bar{q}/\Delta^2$, which is $0.25B_{\rm l}$ for the 10^{-5} model and $0.025B_{\rm l}$ for the 10^{-6} model in the present parameter setting, where Δ is the typical interval of the grid to estimate $E_\parallel$ and we choose $\Delta = 0.1R$. If $E_{\rm cr}$ is taken to be much smaller than $E_{\rm err}$, the pairs are generated in excess and therefore the calculation breaks down immediately because we exceed the limit of the number of particles in our simulation.

3 RESULT

3.1 Quiet solution: without pair creation

As has been shown, if pair creation is suppressed, the electrosphere is composed of electronic domes above the pole, a positronic or ionic equatorial disc and vacuum gaps in the middle latitudes. It takes about one rotation period until the quiet state is achieved with $\alpha = 1$. We also simulate for smaller system charges of $\alpha = 0.75, 0.5, 0.4, 0.3$ with the $\bar{q} = 10^{-6}$ model. The smaller the net charge, the larger the extent of the polar dome (see the left-hand panel of Fig. 4). This tendency has been stated by Krause-Polstorff & Michel (1985b) in their +10 and +4 models, which correspond to our $\alpha = 1$ and 0.4 models, respectively.

The same structures as in KMab are identified with $\alpha \geq 0.4$ in our simulation because the polar dome falls in the light cylinder and therefore it satisfies the condition of rigid constraint for the particle

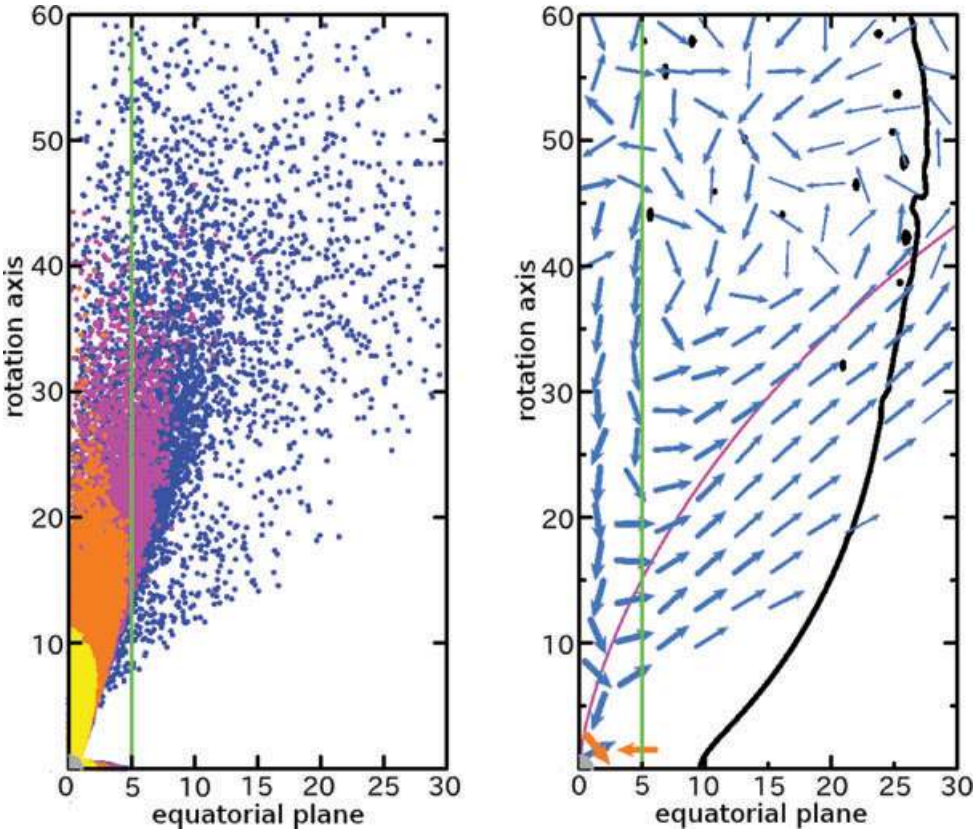

Figure 4. Left-hand panel: the distributions of the particles on the meridional plane with simulated $Q_{\rm sys}$ values, Coloured dots indicate $\alpha = 0.75, 0.5, 0.4, 0.3$ with blue, magenta, orange and yellow, respectively. The light radius is located at $\varpi = 5$ as shown by the green line. Right-hand panel: the current density pattern on the meridional plane for the $\alpha = 0.3$ model. The arrows indicate the direction of the current density of negatively charged particles (blue) and positively charged particles (red). The magenta curve indicates the magnetic field line on the surface with a colatitude of 4°.5. The boundary surface with $E = B$ is represented by the solid curve.

by the dipole magnetic field. But for the model with $\alpha = 0.3$, the static structure changes. The global flow pattern of the particles for the model with $\alpha = 0.3$ is shown in the right-hand panel of Fig. 4. When we choose a model with $\alpha < 0.4$, the polar dome extends beyond the light cylinder and the azimuthal velocity of the particle in the dome increases with the axial distance although the azimuthal velocity is slightly smaller than the corotational velocity. Thus, the Lorentz factor increases close to $\gamma_{\rm d}$ near the light cylinder and then the radiation drag force of the particle makes $\boldsymbol{f}_{\rm rad} \times \boldsymbol{B}$ drift just outside of the light cylinder. Thus, the particles emitted along the polar magnetic field line migrate into the inner magnetic surface if they pass through the light cylinder, and they return to the star at a colatitude higher than their departure point. As a result, there are outflows of negative particles from the polar region, which are bounded by the magnetic surface anchored on the stellar surface at 4°.5. Note that, for our case, the whole charged cloud is still in the magnetic field dominant region ($B > E$). When the outflows go beyond the light cylinder, they move across the inner magnetic surface by the $\boldsymbol{f}_{\rm rad} \times \boldsymbol{B}$ drift and they become inflow by the quadrupole electric field in the vacuum region at the middle latitudes. Thus, the closed poloidal current loops above the pole are formed in several light radii. This is more favourable than the faraway loop of electrons formed because of the attraction of the monopole electric field of the star, as suggested by Jackson (1976). Our results confirmed the same flow pattern of electrons as given by Rylov (1977). Although a part of the edge of the dome has a fast azimuthal velocity, the current density of the dome in the vicinity of the light cylinder is typically $10^{-5}\rho_{\rm GJ,pole}c$, and therefore the modification of the dipole magnetic field should be ignored.

Fig. 5 shows ϕ along two radial directions with $\theta = 30^\circ$ and 90° (equatorial plane), respectively. The former radial line passes through the polar dome while the latter passes through the equatorial disc. It is notable that the derivative $\mathrm{d}\phi/\mathrm{d}\psi$ indicates the angular velocity of the clouds. Along the line with $\theta = 30^\circ$, the electric potential $\phi(\psi)$ follows the corotational $\phi_{\rm co}$ in between A and B in the figure, which correspond to the stellar surface and the surface of the cloud (cloud–vacuum boundary). This indicates that the cloud corotates with the star in the cloud. Along the line with $\theta = 90^\circ$ (equator), the inner part of the disc between D and E follows the corotational $\phi_{\rm co}$, and therefore they show corotation and $E_\parallel = 0$. The point F corresponds to the top of the equatorial disc. Because

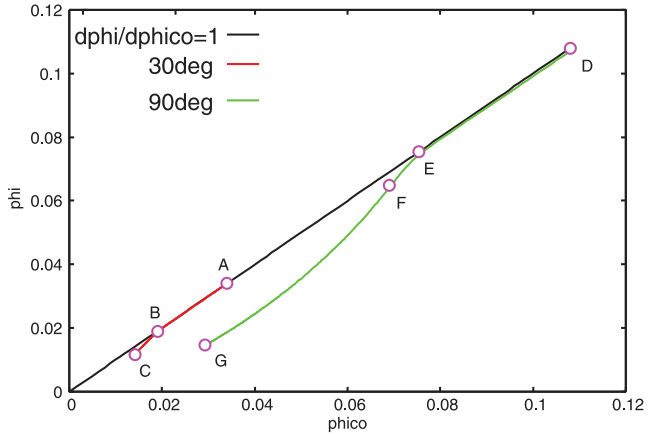

Figure 5. The electrostatic potential ϕ along the radial line with $\theta = 30^\circ$ (A–B–C) and with $\theta = 90^\circ$ (on the equatorial plane) (D–E–F–G) as a function of the magnetic stream function ψ. The solid line indicates the corotational potential $\phi_{\rm co}$.

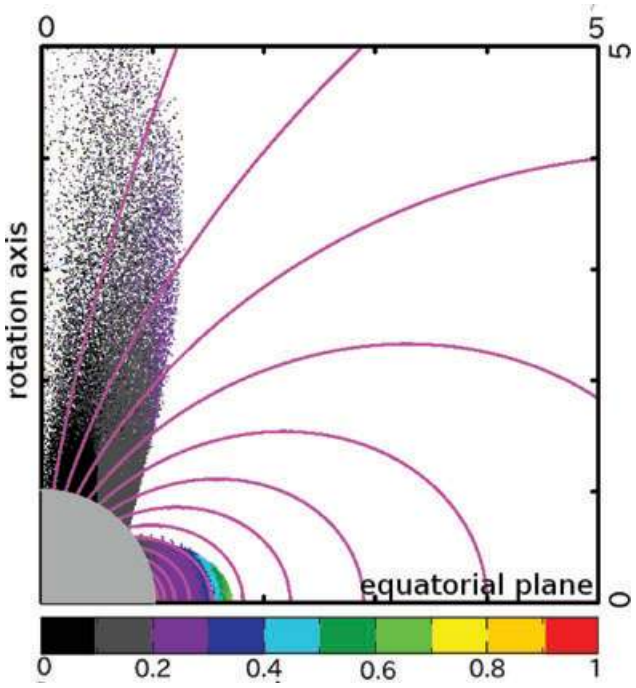

Figure 6. The particles colour-coded for toroidal velocity on the meridional plane. The meaning of the colours is shown in the colour bar just below the equatorial plane, where each colour indicates the corotation speed at each axial distance. The solid curves are dipole magnetic field lines.

$\mathrm{d}\phi/\mathrm{d}\psi > \Omega/c$ in between E and F, the positive charges at the edge of the disc are in supercorotation. This part is connected to the vacuum gaps in the middle latitudes along the magnetic field line. The electric potential in the outer part of the disc decreases faster than the corotational potential. Thus, the supercorotation of the disc top is obtained. The outside of the clouds (between B and C) is a vacuum, and ϕ deviates from $\phi_{\rm co}$, i.e. $E_\parallel$ exists. These features can actually be seen with the velocity of the particle in Fig. 6, i.e. one can see the corotational motion in the polar domes and in the inner part of the disc, and the super-rotation in the outer part of the disc. The azimuthal velocities are not close to the light speed at the top of the equatorial disc, and therefore the radial diffusion mechanism by rotational inertia and radiation drag are negligible in such cases. The outside of the disc (between F and G) is a vacuum.

3.2 Active solution: with pair creation

The steady solutions are obtained in about four rotation periods. To comprehend the trajectories of the particles, we have to know the magnitude relation between electric field and magnetic field and the effect of the drift motion caused by the radiation drag force. When the plasma is in the magnetic field dominant region (MDR), it tends to move along the magnetic surface. However, once it is in the electric field dominant region (EDR), particles are accelerated towards the direction of the electric field. If $E_\perp \sim B$ in the MDR, the velocity of the $\boldsymbol{E} \times \boldsymbol{B}$ drift of the plasma is close to the light speed. Then the radiation drag force for the particle is comparable to the Lorentz force, that is the Lorentz factor of the plasma becomes $\gamma_{\rm d}$, which is given by (28). Such plasma drifts are perpendicular to the magnetic surface by the $\boldsymbol{f}_{\rm rad} \times \boldsymbol{B}$ drift. It is notable that the direction of the $\boldsymbol{f}_{\rm rad} \times \boldsymbol{B}$ drift would be opposite for the two opposite signs of the charge, i.e. the positively charged particle drifts outwards while the negatively charged particle drifts inwards.

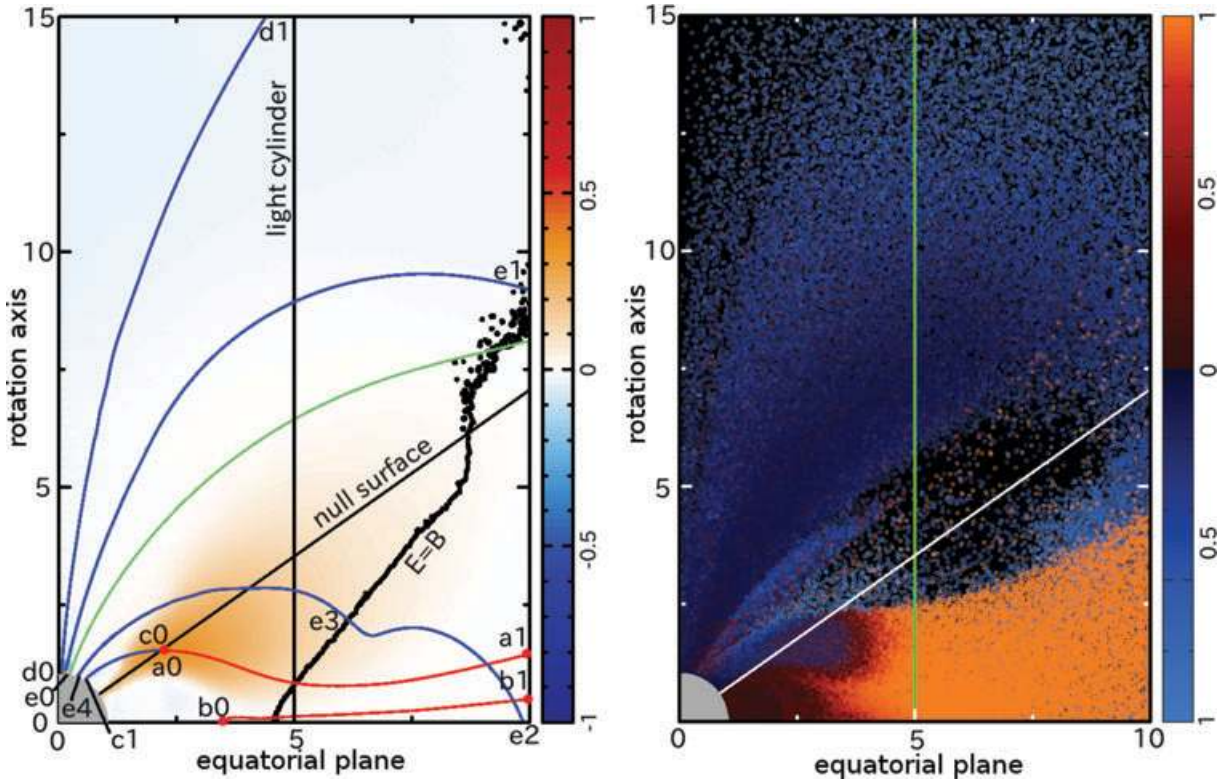

Figure 7. Left-hand panel: typical trajectories of the particles and $E_\parallel$ intensity map; the curves are colour-coded with blue (for the negatively charged particles), red (for the positively charged particles), and the colour map indicates electric field intensity normalized by B_1. The thick solid curve indicates an isosurface with $E = B$, and the green solid curve denotes the equipotential surface with $\phi = 0$. Right-hand panel: Lorentz factor of the particles, which are colour-coded with the Lorentz factor normalized by γ_d. In both panels, the light cylinder is located at $\varpi = 5$ and the line in the middle latitude is the null surface.

In the left-hand panel of Fig. 7, the typical trajectories of particles on the meridional plane are drawn with red and blue curves and the EDR and MDR are bounded by thick curves. The EDR appears around the equatorial plane in a wedge-like shape beyond $\varpi \sim 4.5 = 0.9R_1$ with an opening angle of about 50° from the equatorial plane. Although the EDR appears due to the monopole electric field in the quiet model (Jackson 1976; Rylov 1977), our present model has almost no net charge. The EDR seemed to have been formed by the global structure of the charged cloud, and in particular it would be due to the growing equatorial positively charged disc. An EDR of a similar shape has been discussed by Uzdensky (2003) for the force-free model around the Y-point. The angle between the EDR and the equatorial plane in our result is just wider than their EDR. It is interesting that the structure of the EDR is very similar although our results preclude the force-free approximation and assume the magnetic field to be dipole elsewhere. In the right-hand panel of Fig. 7, the luminous colour-coded particles have Lorentz factor comparable with γ_d, i.e. the radiation drag force for the particles is comparable to the Lorentz force qB_1. They are mainly in the vicinity of the light cylinder. The positively charged particles near the equatorial plane just inside the light cylinder have Lorentz factor γ_d. At the same time, the negatively charged particles in the vicinity of the light cylinder have height above $10R$. The dark colour-coded dots in the right-hand panel of Fig. 7 indicate the non-accelerated particles, i.e. they are corotating with the equatorial disc and the conically shaped polar domes. The background colour of the left-hand panel of Fig. 7 indicates the intensity of $E_\parallel$, which is colour-coded orange ($E_\parallel > 0$), pale blue ($E_\parallel < 0$) and white ($E_\parallel = 0$). On both sides of the outer gap, $E_\parallel$ is shielded and there are corotating charged clouds.

In the left-hand panel of Fig. 7, the flow of positive particles generated in the outer gap goes into the EDR, and it easily goes out beyond the light cylinder ($a_0 \rightarrow a_1$). The plasma at the outer edge of the disc at b_0 has a fast azimuthal velocity, and therefore they are slipped out by $\boldsymbol{f}_{\rm rad} \times \boldsymbol{B}$ drift ($b_0 \rightarrow b_1$). Meanwhile the flow of negative particles generated in the outer gaps moves back to the star ($c_0 \rightarrow c_1$) with colatitude $24^\circ < \theta < 34^\circ$ on the stellar surface, and they are re-emitted from the polar region. The polar flow is separated by the magnetic surface anchored on the stellar surface with a colatitude of 10°, where the equipotential surface of $\phi = 0$ connects up to the star. For the lower colatitude region, it is outflow denoted by $d_0 \rightarrow d_1$. For the other region, it is circulation on the meridional plane, which starts from the polar annulus with colatitude $10^\circ < \theta < 12^\circ$, and returns to the annulus with colatitude $18^\circ < \theta < 24^\circ$ ($e_0 \rightarrow e_1 \rightarrow e_2 \rightarrow e_3 \rightarrow e_4$). On the way through $e_0 \rightarrow e_1$, the flow with fast azimuthal velocity migrates to the inner magnetic surface because of the $\boldsymbol{f}_{\rm rad} \times \boldsymbol{B}$ drift. Once it moves into the EDR, it is accelerated and passes over the equatorial plane. Because of the symmetry about the equatorial plane, the flow with the same trajectory in the opposite hemisphere returns from e_2, then it moves into the MDR ($e_2 \rightarrow e_3$). Thus, it returns along a magnetic field line just outside the pair-creating region in the middle latitude ($e_3 \rightarrow e_4$).

The overhead view of the steady solution is shown in Fig. 8. The intensity ratio of the dipole magnetic field and the magnetic field made of the magnetospheric current in the steady state are drawn

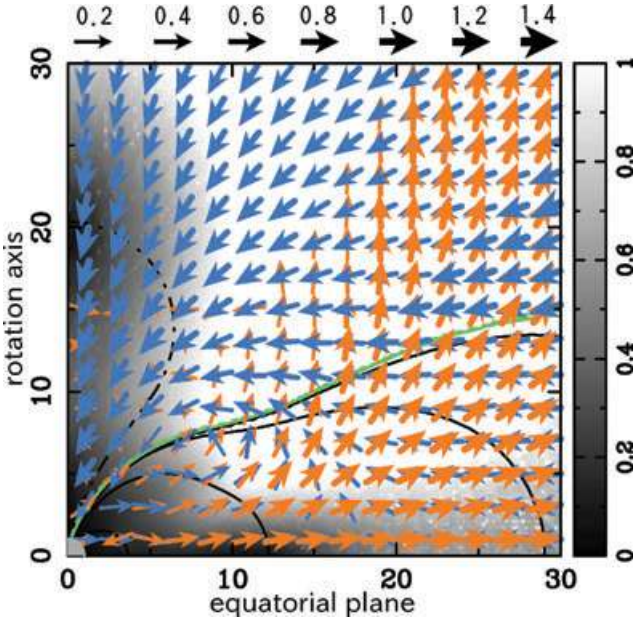

Figure 8. The arrows indicate the current density made of positive charge (orange) and negative charge (cyan), which are normalized by $\Omega B/(2\pi)$. The intensity ratio of the dipole magnetic field and the magnetic field made of the magnetospheric current is shown by the grey-scale colour-coded map, that is $|B_q|/|B_\mathrm{d}|$. The curves are electrostatic equipotentials normalized by ϕ_max with a common logarithm, where $\phi = 0$ is coloured green; the solid curve indicates $\phi > 0$ and the dashed curve indicates $\phi < 0$.

as a grey-scale map. The current density normalized by $\Omega B/(2\pi)$ on the meridian plane is drawn with colour-coded arrows and the electrostatic equipotentials normalized by ϕ_eff are drawn as curves. The green curves indicate that the value of the equipotential is zero. The value of the potential is negative in the lower colatitude region and is positive in the higher colatitude region. The contour level is incremented by -3, -2, -1, 0 with common logarithm from the zero-equipotential surface for both signs of potentials. It shows that the assumption of a dipole magnetic field is valid in the light cylinder and especially around the equatorial plane, although the magnetic field made by the magnetospheric current is comparable to the dipole field in the middle latitude about beyond $3R_\mathrm{l}$, where magnetic flux is modified to be opened. The circulation pattern of the flow in the present result would turn downwards if the modification of the magnetic field were taken into account. The magnetic field made by the magnetospheric current is trivial inside the light cylinder; in other words, the structure of the outer gaps and pair-creation rate should not be affected in the present model if the modification of the dipole magnetic field is taken into account. In contrast, outside several light radii, the magnetic field made by the magnetospheric current is comparable to the dipole magnetic field. However, it is almost in the EDR, and therefore the particle flow is controlled by the electric field. Concerning the global structure of the current and equipotential surfaces, the negatively charged particles flowed out at a lower latitude and the positively charged particles flowed out at a higher latitude. However, the system of charge in our results is almost neutral, that is the monopole electric field would not prevent a reverse charged outflow to a great distance. Eventually, both outflows have enough kinetic energy larger than the potential energy at the outer boundary, and therefore they can reach infinity beyond the outer boundary. Inside the sphere with a radius of about $3R_\mathrm{l}$, there are poloidal current loops caused by $\boldsymbol{f}_\mathrm{rad} \times \boldsymbol{B}$ drift from equatorial plane to the pole, which consist mainly of a negatively charged flow. In our previous paper (WS), the parameter of radiation drag force, η, is taken to be unity so that the circulation of charges of both signs caused by the $\boldsymbol{f}_\mathrm{rad} \times \boldsymbol{B}$ drift is exaggerated. In the results of the present paper, few positive charges return although the poloidal current structure is similar to that in WS.

4 DISCUSSION

4.1 Comparison with the quiet solution

Smith et al. (2001) concluded that their result for the axisymmetric magnetosphere is quiet because the pair plasma which moves along the dipole magnetic field lines screens out $E_\parallel$ in the outer gaps and therefore the pair creation is stopped. They implied that the activity of a pulsar is caused essentially by obliqueness (see also Michel 2004). Although a similar screening of the outer gaps is shown in our simulation, the intensity of the electric field is maintained in order to generate pair plasma. We note that our active solution arises from taking a smaller threshold intensity of electric field for pair creation than Smith et al. (2001), and from solving the equation of motion for each particle without the assumption of restraint of plasma along the dipole magnetic field line. As a result, we have shown that if the radiation drag of the particle and the supply of the pair plasma in the gaps are performed, the quiet system should be broken and should migrate over to the active system with gaps and to outflows of both signs of the plasmas; nevertheless, the rate of pair creation is taken to be small as the modification of the dipole magnetic field is omitted. Some fraction of the positive charge generated in the outer gaps accumulates in the equatorial plane, and therefore the super-rotating disc grows and the azimuthal velocity increases, and then the Lorentz factor increases as the light cylinder reaches some fraction of γ_d. The particles at the cusp of the disc start to leak out due to the $\boldsymbol{f}_\mathrm{rad} \times \boldsymbol{B}$ drift. If the potential drop in the outer gap is f as a fraction of the effective voltage, the trans-field drift would take place beyond $(1 - f)R_l$, i.e. it is likely that radiation drag causes trans-field drift motion within the light cylinder. As has been shown, this effect creates an outflow of positively charged particles even if the dipole magnetic field is closed, and it is favourable to keep the outer gaps.

As diocotron instability of a differentially rotating disc is pointed out by Spitkovsky (2004), Pétri et al. (2002b) and Pétri (2007), the leakage from the edge of the disc is realized after several rotation periods in our simulation. Although it prompts the decrease of the charge from the system even if all particles are trapped in a closed magnetic surface or pair creation is suppressed, the rate of growth of the disc decreases when the disc grows in the vicinity of the light cylinders and when the decrease of charge is trivial compared to the total charge of the disc. We formulated simulations to confirm how the diocotron instability affects the global structure of the disc over 20 rotation periods for the pair-starved electrosphere, but these simulations are barely fit to be carried out in our present environment. At least we realized that diffusion by the diocotron instability was not so significant in such a time-scale, although the diffusion by $\boldsymbol{f}_\mathrm{rad} \times \boldsymbol{B}$ changes the quiet electrosphere in several rotation periods. Note that the growth of the disc is caused by the pair-created positive charges in the outer gaps and the main component of the leakage of the disc is the $\boldsymbol{f}_\mathrm{rad} \times \boldsymbol{B}$ drift of the particle in our simulation, and even the loss of the positive charge from the edge of the disc is much lower than the outflow from the outer gaps to the EDR (see the left-hand panel of Fig. 7, $a_0 \rightarrow a_1$).

If plasma is supplied in copious amounts to the equatorial disc from the outer gaps, another important issue remains the region, the so-called Y-point, which is expected to have an electric field larger than the magnetic field in force-free theory (Uzdensky 2003). In the next paper, we will treat higher rates of pair creation, for which modification of the magnetic field becomes significant in the vicinity of the light cylinder. Then, some poloidal magnetic flux is opened and toroidal magnetic field would be antiparallel on both sides of the equatorial plane in which the dissipation of the magnetic field is expected to accelerate the particles. Thus, trans-field leakage of the particles around the Y-point is a very interesting issue, but we postpone further discussions of it until simulations with higher rates of pair creation are performed.

4.2 Formation process of steady solution

Although the steady solution is stated in Section 3.2, here we discuss it as a stage of the active solution. Once pair creation begins, the pair plasmas are generated at first in the middle latitudes in which $E_\parallel$ is stronger than $E_{\rm cr}$ (see Fig. 3). The pairs created in the outer gaps are immediately separated in opposite directions along a magnetic field line by $E_\parallel$. Then, most of the positive charges move into the EDR to form an outflow. At the same time, the negative charges move inwards. They return to the star and are re-emitted from the polar regions so that the height of the dome increases. The outflow of the positive particles causes a significant change to the global structure: the system charge, which is initially assumed to be positive, is reduced. As a result, the potential of the polar region becomes negative, and the lower latitude part of the polar domes becomes the location of outflow. The other half of the polar dome grows and crosses over the light cylinder. The Lorentz factor of the plasma increases to bring about a trans-field motion by radiation drag force. It is notable that the negative charges obtain kinetic energy if they drift towards inner magnetic surfaces. Some of the particles become the outflow if the kinetic energy is larger than the potential energy at the outer boundary, and therefore the separatrix of the negatively charged flow is created on the equator with $3R_{\rm l}$ in the present result, although it is set on the equator with about $8R_{\rm l}$ in previous work. The difference might arise from the resolution of the charge; exploring in detail the mechanism of formation of the separatrix with a modification of the magnetic field will need additional simulation in future work. Thus, a steady state is found in equal losses of both particle species and the lost particles are supplied by the outer gaps.

In our simulation, we demonstrate the generation of particles intermittently in some periods, $\bar{\tau}_{\rm pr} = 0.1,\ 0.2,\ 1.0,\ 2.0$, for the pair creation and a fixed period $\bar{\tau}_{\rm po} = 0.1$ for the popping from the stellar surface. All steady results had the same geometry of the charged clouds, which were an equatorial disc of positive charge, polar domes of negative charge and outflows of both signs. Thus, the choice of $\bar{\tau}_{\rm pr}$ and $\bar{\tau}_{\rm po}$ in the present simulation does not affect the results. We checked that if the lower system charge solution without pair creation is chosen as an initial condition, then the same result was obtained qualitatively.

4.3 Structure of outer gaps

Here we discuss the structure of the outer gaps in the context of our results. For the discussion, the structure of the electrostatic potential and the intensity of $E_\parallel$ in the pair-creating region is prepared for our active solutions, where we obtained the solution with several pair creation rates in the simulation. Note that in our simulation, $E_{\rm cr}$ has been assumed to be larger than a parameter of emission of γ-rays in reality; in other words, the pair-creation rate has been underestimated in our simulation. For this reason, the size of the pair-creating region is expanded and therefore the geometry of the outer gaps is not revealed quantitatively from our simulation. Although the structure of the outer gaps that have demonstrated a lower rate of pair creation contains some fraction of an artefact, the results imply how the transition of the magnetosphere from the active state to the quiet state is realized with time for the pulsar, that is the evolution of the magnetosphere with the abundance of the pair plasma, which decreases with the age of the pulsar.

Another important point is that we can suggest the possibility of coexistence for the polar cap and outer gap by comparing with the deviation from the force-free magnetosphere. If a force-free condition is satisfied elsewhere, we give the corotational potential under a dipole magnetic field assumption,

$$\phi_{\rm co} = \frac{\Omega\mu \sin^2\theta}{cr}. \tag{29}$$

Then the non-corotational potential is defined as $\phi_{\rm nco} \equiv \phi - \phi_{\rm co}$. Fig. 9 shows the non-corotational potential with a colour map and pair-creating region with contour for the B_0 model on the meridional plane. The pair-creating region becomes dramatically small compared with the initial state in our simulation, but the intensity of the $E_\parallel$ in steady state remains greater than $E_{\rm cr}$ in the contour. Eventually, the pair-creating regions remained in the middle latitudes and just above the poles. We do not distinguish between the processes of pair creation in the present simulation, which are photon–photon collision and magnetic pair creation, and therefore the rate of pair creation is only proportional to the product of the intensity of $E_\parallel$ and the volume of the gap. Thus, the supply of plasma generated in the polar pair-creating region was trivial compared with that from the outer gaps, that is, our simulation underestimated the effect of shielding by pair plasma on magnetic pair creation in the polar cap. As Takata, Wang & Cheng (2010) have suggested that a new outer gap closure mechanism by magnetic pair creation near the stellar surface is significant in realizing the observed features of γ-ray

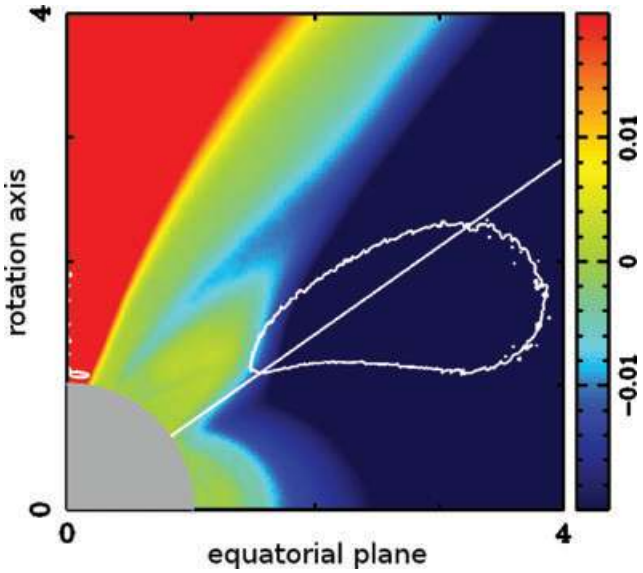

Figure 9. Distribution of non-corotational potential on the meridional plane; the contour indicates an isoline with $E_\parallel = E_{\rm c}$. The colour of the map is normalized by 2 per cent of the open field line voltage $\phi_{\rm eff}$. The line at middle latitude is the null surface.

pulsars, the effect of the different types of pair creation should be investigated in future work.

In Fig. 9, the equatorial disc and polar domes have a domain in which $\phi_{\rm nco}$ has a deviation less than $0.01\phi_{\rm eff}$. They do not constitute the accelerating region of the particles; they form the dead zone. For our result, the existence of the dead zone provides inspiration. Usually, the conventional polar cap and the outer gap are defined on the last closed field line in the GJ model and the poloidal current in the gaps has the opposite direction, and therefore the gaps cannot coexist. In the present results, the dead zone in the equatorial disc has reduced in the light cylinder, and the effective last closed line has migrated to a higher colatitude and the one in the polar dome cuts down the radius of the cone in which particles outflow. Note that the dead zones divide the last closed field line and would be able to coexist with the polar cap and outer gap on different magnetic surfaces. The poloidal current travels into the polar region of the stellar surface of the lower colatitude side of the polar dead zone, migrates to the magnetic surface with a higher colatitude and passes through the outer gaps. The current causes poloidal circulation beyond the light cylinder. We do not demonstrate detailed processes of pair creation and do not simulate with enough accuracy to resolve the size of the polar caps in the present results, therefore it is not clear whether or not the current from the polar cap is a necessary condition. This interesting result should be discussed in future work.

For the limited robustness of our gap–wind solution, we carried out models of some rates of pair creation. We investigated and confirmed that $E_\parallel$ in the gap saturates with a constant value for all the steady states. Fig. 10 shows the saturated intensities of $E_\parallel$ on the null surface in all simulations. All the results have regions whose $E_\parallel$ was larger than $E_{\rm cr}$ on the null surface. The width of the base of the bell-shaped curve with $E_\parallel/E_{\rm cr} = 1$ indicates a typical size of the pair-creating region on the null surface. There is a tendency for the higher pair creation rate model ($A_0 \rightarrow A_1 \rightarrow A_2 \rightarrow A_3$), which is parametrized by the frequency of pair creation $\bar{t}_{\rm pr}$, to decrease both the size of the pair-creating region and the intensity of $E_\parallel$. The saturated intensities are maintained just above $E_{\rm cr}$. When $E_{\rm cr}$ was taken to be a much smaller value ($A_0 \rightarrow A_4 \rightarrow A_5$), the pair-creating region decreased in the same way and the saturated electric field intensity was just higher than $E_{\rm cr}$. In the lower $E_{\rm cr}$ model, the particles tended to screen out the gaps near the star although the outer edge of the pair-creating region does not change. This indicates that the inner boundary of the outer gap, which has a beak-like shape

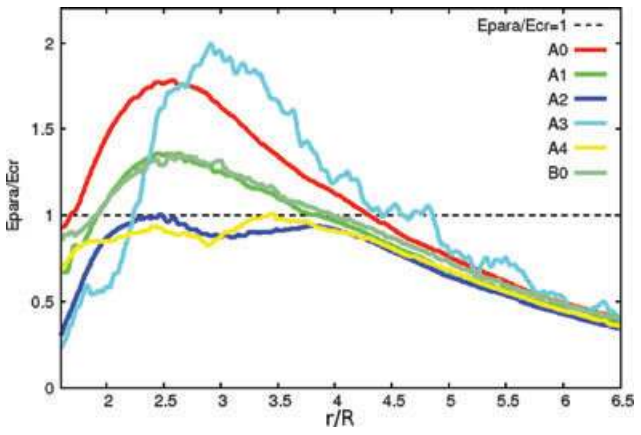

Figure 10. The curves are $E_\parallel$ normalized by $E_{\rm cr}$ on the null surface. The horizontal axis indicates distance normalized by the stellar radius along the null surface. The key indicates the types of simulation referred to in Table 1.

on the meridional plane, would not be connected to the star if we could carry out a much lower $E_{\rm cr}$ model. As Fig. 7 shows, the inner edge of the outer gap would be refined just outside the outer edge of the dead zone which is roughly defined as a magnetic field line anchored on the stellar surface at 32° in our simulation. The inner boundary is slightly inside compared with that of the conventional outer gap model on the null surface. This agrees with the work of Takata, Shibata & Hirotani (2004) in which they have calculated the electrodynamics of an outer gap on the meridional plane with an assumed external current, then as the current density increases, the inner boundary of the outer gap shifts towards the stellar surface. As previously explained, since the main path of the equatorial outflow exists outside the dead zone, the outer gap structure in our simulation can be maintained steadily.

We emphasize that the thickness of the pair-creating region traversing the dipole magnetic surface would be related to the size of the region in which leakage of the disc particles takes place ($\sim fR_l$), because the field-aligned potential drop in the outer gap controls the super-rotation of the disc. Phenomenologically postulated, the thicknesses of the outer gaps for old pulsars are shown by Zhang & Cheng (1997), in which they point out that the effect of the finite mean free path of the γ-rays for pair creation is important for defining the thickness of the outer gap. In addition to this, the direction of the γ-rays would be important to define the geometry of the outer gap because the particles have fast azimuthal motion in the gaps near the light cylinder, and therefore the γ-rays are emitted in the azimuthal direction and the path of the γ-rays should be considered with three-dimensional geometry. We should consider the mean free path of γ-rays for pair creation with a three-dimensional model in future work.

4.4 Polar gap

The polar cap accelerator has been an outstanding issue in the context of understanding radio emissions. We find a potential drop just above the stellar surface in our simulation in a fashion similar to WS. The mechanism is very simple: in a steady state the negative charges created in the outer gap flow back to the star, and therefore an equal amount of negative charges should be emitted for steadiness. Then, the potential drop in the polar region of the stellar surface controls the polar flow of negative particles, which is represented by

$$\phi(\boldsymbol{R}) = \frac{\mu\Omega}{cR}\left(\sin^2\theta - \frac{2}{3}\right) + \frac{Q_{\rm sys}}{R} - \sum_{i=1}^{n}\frac{q_i}{R}\left(1 - \frac{R}{r_i}\right). \qquad (30)$$

In all the results of our simulations, $\phi_{\rm pole}$ becomes slightly negative, and therefore the negative particles are pushed and they easily escape to infinity. Implied by (30), this potential is maintained by a balance between the numbers of negative and positive particles in the magnetosphere (the second term) and $Q_{\rm sys}$ (the third term). Thus, we see that in the steady state $Q_{\rm sys}$ is determined so that the losses of negative and positive particles are balanced. This indicates that the polar caps have a close correlation with the injection of electrons from the outer gaps. In the present case, the rate of emitted particles from the polar region is less than what would be capable of shielding the electric field above the pole, that is the current density from the pole is less than $\rho_{\rm GJ}c$, and therefore the unscreened potential increases gradually along the polar magnetic field lines. In other words, this potential drop above the pole is not a conventional polar cap because the electric field is not shielded in a finite distance near the stellar surface. There is a very interesting question of whether a potential drop near the polar region

remains if enough electrons return from the outer gaps and are re-emitted from the pole, or generated in the polar cap and then the emitted particles should form a space charge limited flow (Arons & Scharlemann 1979); however, our simulation particles have a large inertia length of 3 per cent of the stellar radius, and therefore the detailed structure might not be demonstrated. Note that our simulation contains an artificial polar gap arising from the intermittent emission of particles on the stellar surface, which is in the range of $t_{\rm po}c = 0.1R$ at maximum. Unfortunately, it is difficult to take a much smaller value of $t_{\rm po}$ in the present parameter setting. Thus, it is not clear whether the polar electric field is shielded on the pole if the pair-creation process is considered in detail, and whether or not the polar electric flow needs pair creation in polar cap. As shown by Hirotani, Harding & Shibata (2003), the current from the polar cap has a significant effect on the outer gap electrodynamics; to discuss the possibility of the existence of polar caps linked with the outer gaps, a combination of localized simulation and global simulation would be needed.

5 CONCLUSION

For an axisymmetric pulsar magnetosphere, pair creation in the outer gaps results in an expansion of the rotating electrosphere and a trans-field drift motion due to radiation drag force near and beyond the light cylinder. Eventually, a steady state is achieved with the outflow of both particle species and the global current loop on the meridional plane. We confirmed that the pair-starved static electrosphere shifts to the steady structure via the pair plasma in the gaps. The pair creation plays the important role of metamorphosing from the static electrosphere to the steady structure; nevertheless, the pair-creation rate is artificially suppressed in our present model. For a more detailed discussion of the structure of the magnetosphere, the mean free path of the pair creation, which is important for old pulsars having thick outer gaps, needs to be considered to discuss the structure of the gap quantitatively. Additionally, a higher pair creation rate case should be simulated, so that the modification of the magnetic field from dipolar changes both the pattern of outflow of the plasma and the structure of the gaps. Thus, our model can be developed to consider pulsar magnetospheres including much more pair plasma in the next paper.

ACKNOWLEDGMENTS

We would like to thank Jumpei Takata, Hiroyuki Takahashi, Syota Kisaka and the anonymous referee for discussions and many helpful comments on the manuscript. Numerical simulations were carried out on the MUV system at the Center for Computational Astrophysics, National Astronomical Observatory, Japan.

REFERENCES

Abdo A. A. et al., 2009a, Sci, 325, 840
Abdo A. A. et al., 2009b, Sci, 325, 848
Abdo A. A. et al., 2009c, ApJ, 696, 1084
Abdo A. A. et al., 2010, ApJS, 187, 460
Aliu E. et al., MAGIC Collaboration, 2008, Sci, 322, 1221
Arons J., Scharlemann E. T., 1979, ApJ, 231, 854
Becker W., Trüemper J., 1997, A&A, 326, 682
Bucciantini N., Thompson T. A., Arons J., Quataert E., Del Zanna L., 2006, MNRAS, 368, 1717
Cheng K. S., Ho C., Ruderman M., 1986a, ApJ, 300, 500
Cheng K. S., Ho C., Ruderman M., 1986b, ApJ, 300, 522
Daugherty J. K., Harding A. K., 1996, ApJ, 458, 278
de Jager O. C., Djannati-Ataï A., 2008, in Becker W., ed., Springer Lecture Notes on Neutron Stars and Pulsars: 40 yr After Their Discovery. Springer, Berlin, in press (arXiv:0803.0116)
Goldreich P., Julian W. H., 1969, ApJ, 157, 869 (GJ)
Harding A. K., Muslimov A. G., 2002, ApJ, 568, 862
Hirotani K., Shibata S., 1999, MNRAS, 308, 54
Hirotani K., Harding A. K., Shibata S., 2003, ApJ, 591, 334
Hobbs G. et al., 2004, MNRAS, 352, 1439
Holloway N. J., 1973, Nat, 246, 6
Jackson E. A., 1976, ApJ, 206, 831
Kargaltsev O., Pavlov G. G., 2008, Proc. AIP Conf. 983, 171
Kennel C. F., Coroniti F. V., 1984a, ApJ, 283, 694
Kennel C. F., Coroniti F. V., 1984b, ApJ, 283, 710
Kirk J. G., Skjæraasen O., Gallant Y. A., 2002, A&A, 388, L29
Komissarov S. S., 2006, MNRAS, 367, 19
Krause-Polstorff J., Michel F. C., 1985a, MNRAS, 213, 43P
Krause-Polstorff J., Michel F. C., 1985b, A&A, 144, 72
Makino J., Hiraki K., Inaba M., 2007, in Proc. ACM/IEEE Conference. ACM, New York, p. 1
McKinney J. C., 2006a, MNRAS, 367, 1797
McKinney J. C., 2006b, MNRAS, 368, L30
Michel F. C., 2004, Advances Space Res., 33, 542
Michel F. C., Smith I. A., 2001, Rev. Mex. Astron. Astrofis. 10, 168
Muslimov A. G., Harding A. K., 2003, ApJ, 588, 430
Muslimov A. G., Harding A. K., 2004, ApJ, 606, 1143
Nel H. I. et al., 1996, ApJ, 465, 898
Pétri J., 2007, A&A, 469, 843
Pétri J., Heyvaerts J., Bonazzola S., 2002a, A&A, 384, 414
Pétri J., Heyvaerts J., Bonazzola S., 2002b, A&A, 387, 520
Possenti A., Cerutti R., Colpi M., Mereghetti S., 2002, A&A, 387, 993
Rees M. J., Gunn J. E., 1974, MNRAS, 167, 1
Romani R. W., 1996, ApJ, 470, 469
Ruderman M. A., Sutherland P. G., 1975, ApJ, 196, 51
Rylov I. A., 1977, Ap&SS, 51, 59
Smith I. A., Michel F. C., Thacker P. D., 2001, MNRAS, 322, 209
Spitkovsky A., 2004, in Camilo F., Gaensler B. M., eds, Proc. IAU Symp. 218, Young Neutron Stars and Their Environments. Kluwer, Dordrecht, p. 357
Takata J., Shibata S., Hirotani K., 2004, MNRAS, 354, 1120
Takata J., Shibata S., Hirotani K., Chang H.-K., 2006, MNRAS, 366, 1310
Takata J., Wang Y., Cheng K. S., 2010, ApJ, 715, 1318
Uzdensky D. A., 2003, ApJ, 598, 446
Wada T., Shibata S., 2007, MNRAS, 376, 1460 (WS)
Zhang L., Cheng K. S., 1997, ApJ, 487, 370
Zhang B., Harding A. K., 2000, ApJ, 532, 1150

This paper has been typeset from a TEX/LATEX file prepared by the author.